Available online at www.sciencedirect.com
ScienceDirect
International Journal of Heat and Fluid Flow 29 (2008) 1113–1124
International Journal of HEAT AND FLUID FLOW
www.elsevier.com/locate/ijhff

Measurements of density profile evolution during the stably-stratified filling of an open enclosure

Constantine M. Tarawneh [a], K.O. Homan [b,*]

[a] Department of Mechanical Engineering, University of Texas-Pan American, Edinburg, TX 78539-2999, United States
[b] Department of Mechanical and Aerospace Engineering, Missouri University of Science and Technology, (formerly University of Missouri-Rolla), Rolla, MO 65409-0050, United States

Received 11 July 2007; received in revised form 25 January 2008; accepted 28 January 2008
Available online 24 March 2008

Abstract

The stably-stratified filling of an open enclosure produces an interfacial gradient layer which is transported through the enclosure with the bulk flow. The evolution of this interfacial layer is strongly time-dependent and is driven by the nature of the interaction between the internal gravity waves and the inlet-driven interfacial shear. Measurements of density profile evolution have been completed for a rectangular enclosure with a single corner inlet and density variation produced by saline concentration. This system serves as a mass transfer analog to large-scale, thermally-stratified energy storage devices, preserving dynamic similitude in a laboratory-scale system. The experiments covered jet Reynolds numbers of 200–2200 and Froude numbers of 0.06–0.6 in an enclosure with a width 23 times the jet inlet height. The density profiles are seen to be strongly asymmetric and exhibit growth rates significantly different than due to simple one-dimensional molecular diffusion. In addition, shadowgraph and hydrogen bubble visualizations of the density and velocity fields in the gradient layer show the persistence of complex multi-dimensional flow structure even at relatively late stages of the filling process when the gradient layer has been transported well away from the enclosure inlet. The evolution of the vertical density profile has been compared quantitatively to a quasi one-dimensional model based upon empirical diffusivity coefficients.

Keywords: Mixed convection; Stratified flow; Interfacial mixing; Thermal storage

1. Introduction

Convective transport in enclosures is important to a wide array of engineering applications including energy transfer within buildings, cycling of thermal storage vessels, crystal growth from the melt, as well as reservoir dynamics, among others. Major distinctions between the various types of enclosure flows are whether the system is open or closed, steady or unsteady, and whether the energy transfer to the system is via surface heat flux or surface shear stress. A large portion of previous effort, particularly those motivated by solar applications, has been directed toward steady-state transport within closed enclosures, i.e. no mass flow through the enclosure, with energy transfer in the form of surface heat flux. For the simplest flow geometries, the resulting flow consists of boundary layers at the closed surfaces coupled to an interior core flow. The largest gradients occur in the surface boundary layers. Steady and unsteady results for these cases have been reviewed elsewhere (Anderson and Kreith, 1987; Catton, 1978; Hyun, 1994; Ostrach, 1982). In contrast, for closed systems which are initially stratified and have energy transfer driven by shear stress at a free surface, the energy transfer causes a sharpening of the internal gradient layer due to entrainment (Turner, 1979). Such configurations are particularly important in geophysical applications where the vertical transport of nutrients, and possibly pollutants, is important to biological processes. Open enclosure flows encompass a vast array of possible combinations since

* Corresponding author. Tel.: +1 573 341 6622; fax: +1 573 341 4115.
E-mail address: khoman@umr.edu (K.O. Homan).

0142-727X/$ - see front matter © 2008 Elsevier Inc. All rights reserved.
doi:10.1016/j.ijheatfluidflow.2008.01.012

Nomenclature

Dimensional variables are denoted by a hat e.g. $\hat{t}$

Romans

A	area
b	model parameter, see Eq. (25)
c	constant
f	function, see Eq. (23)
Fr	Froude number, see Eq. (2)
g	acceleration of gravity
g'	reduced gravity
H	test section height
h	inlet height
L	test section length
l	length
N	Brunt–Vasaila frequency, see Eq. (10)
Pe	Péclet number, see Eq. (1)
P	period
r	model coefficient, see Eq. (21)
Re	Reynolds number, see Eq. (3)
T	temperature
t	time
$\bar{u}_i$	area-average inlet velocity
V	voltage
v_b	bulk vertical velocity
$\dot{V}$	volumetric flow rate
W	test section width
x, y, z	spatial coordinates

Greek symbols

α_m	molecular diffusivity
δ	gradient layer thickness
δ^*	empirical gradient layer thickness
ε	convective diffusivity
κ	mixing factor, see Eq. (17)
$\tilde{\kappa}$	mixing factor coefficient, see Eq. (25)
v	kinematic viscosity
ρ	density

Subscripts and superscripts

a	average, averaging
c	convective
e	edge
f	fill line
h	high
i	inlet side of gradient layer
l	low or lower side of gradient layer
n	refers to either l or u
o	outlet side of gradient layer
p	probe
r	relative, ratio
u	upper side of gradient layer

energy transfer may occur not only by surface fluxes but also by bulk flow through the enclosures. Examples include mixed convection in open enclosures (Neiswanger et al., 1987), fires, and reservoir flows.

The present investigation focuses on an open enclosure flow in which the internal dynamics are dominated by the mass transport through the enclosure and not the surface energy transfer. Motivated by applications to large-scale thermal energy storage vessels, the present study examines the stably-stratified filling of an open enclosure by a relatively dense inflow at a lower corner of the enclosure. When the vessel initially contains a fluid of uniform, relatively lower density, the filling process produces a gradient layer which is transported through the enclosure with the bulk flow. The evolution of this gradient layer is critical to the resulting thermal performance of the storage vessel as any thermal mixing corresponds to a loss of heat transfer potential (or thermodynamic availability) (Ji and Homan, 2006, 2007).

The basic physical configuration being investigated has been extensively studied in the context of heat storage (Lavan and Thompson, 1977; Mavros et al., 1994), particularly for solar applications. However, such applications correspond to relatively low Péclet numbers due to the small physical scale of the storage vessels and to relatively low Froude numbers due to the large temperature differences typical of solar thermal systems. The objective of the present study was to investigate empirically the convective transport dynamics active at Péclet and Froude (or Richardson) numbers representative of large-scale thermal storage applications. Since the temperature differences in these systems are much smaller than in typical small-scale heat storage applications, the strength of gravity as a stabilizing effect is significantly reduced. The measurements of local density and visualizations of the unsteady density and flow fields were completed in an experimental facility using salt concentration as a mass transfer analog for thermal energy transfer. The results have also been used to compute empirical parameters which allow estimation of the importance of convective transport relative to molecular diffusion in these devices. One immediate application of the present results is to the design and operation of building energy systems incorporating large-scale, stratified thermal energy storage devices.

2. Experimental apparatus and procedure

2.1. Test section

The experimental apparatus consisted of a test section constructed of Plexiglas with an aluminum frame to pro-

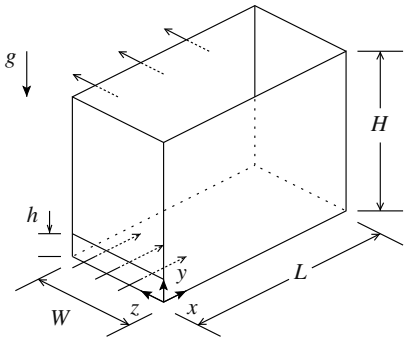

Fig. 1. Schematic of the test section used for the open enclosure experiments.

vide the necessary structural integrity. The test section is illustrated in Fig. 1.

The internal dimensions of the test section are 118 cm in the direction of the inflow (L), 118 cm in height (H) to the free surface and 24 cm width in the cross-flow direction (W). The inlet slot at the lower corner of the test section is slightly narrower than the internal test section width, 23 cm, and has a height of 5 cm (h). The test section is operated such that the volume flow rate into the test section is balanced by the exit flow rate. The outflow leaves the test section via three 2 cm holes located at the top of the test section and connected to an outflow tank with flexible tubing. The overall system schematic is shown in Fig. 2.

The entrance to the test section is a rectangular channel 24 cm long in the direction of flow which provides a transition from two 3.2 cm PVC pipes to the inlet slot. Dye visualization experiments were performed to verify that the flow across the width of the inlet slot was essentially uniform.

The overall flow schematic, as illustrated in Fig. 2, is designed for batch operation. The system consists of two high-density polyethylene (HDPE) tanks in which the high density inflow solution and the low density solution used to initially fill the test section are prepared. A pump and head tank system are used to provide a constant flow rate into the test section. The head tank is constructed of Plexiglas and has a dividing panel which separates the interior into two volumes, one connected to the test section, the other returning to the inflow solution tank. The head tank was positioned approximately 4.3 m above the bottom of the test section. To accommodate the desired range of flow rates, the flow from the head tank to the test section is directed through one of three rotameters, each of which have been calibrated with the standard time-and-catch method. The maximum flow rate which could be maintained with the described systems was 31.4 liters per minute.

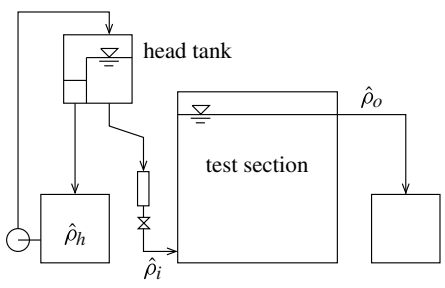

Fig. 2. Flow schematic for the transient filling process.

The local density was measured with a commercially-available conductivity probe constructed as described in Head (1983). The instrument produces an output voltage which is linearly proportional to local solution conductivity and has a spatial resolution approximately 1 mm with a temporal response of -3 dB at 800 Hz. The probe is mounted in a 6.4 mm stainless steel shaft of 1.4 m length to enable movement throughout the test section depth. Calibration of the conductivity probe must be performed prior to the start of each experiment. The calibration process consists of setting the instrument gain for a calibration solution of specific gravity (or conductivity) higher than that which is to be measured. A reference saline solution of specific gravity 1.014 was used for this upper calibration point. A saline solution with a specific gravity of 1.011 was, in all cases, used as the high density inflow to the test section. The specific gravity (relative to water at 15.6 °C) was measured with a hydrometer having a bias and precision uncertainty of 0.0005 and 0.00025, respectively.

The conductivity probe was positioned vertically in the test section with a linear slide having a stroke length of 1.125 m and a pitch of 5 mm. The movement of the slide was produced by a stepper motor controlled by software operating on a dedicated PC. The step angle was 1.8°, giving 200 steps per revolution. The maximum speed was 1400 steps per second which gives a probe velocity of 3.5 cm/s. A divide-by-n circuit was used to synchronize the data collection process with the motion of the stepper motor. In this way, the measured local density can be directly related to the vertical position of the probe.

2.2. Experimental procedure

The two HDPE tanks were filled with tap water and the temperature adjusted to within 0.2 °C. Salt was added to the inflow tanks to produce an inflow solution of the desired density. The pump was then turned on and the inflow solution circulated between the inflow tank and the head tank to ensure thorough mixing. The valve to the test section was opened and the flow rate adjusted. The valves immediately preceding the entrance region were then closed and the test section flushed with tap water. The test section was then filled with the low density solution from the second HDPE tank. At this point, the probe was calibrated with a solution acclimated to the high and low density solutions. Finally, the probe was moved into the position appropriate for the type of experiment to be performed.

The conductivity data was collected in two basic types of experiments: one, fixed probe experiments in which the

probe was kept at a fixed position $y_p = \hat{y}_p/H = 0.65$ throughout the duration of the experiment, and two, moving probe experiments in which the probe was moved rapidly down through the gradient layer. In this latter type of experiment, the probe was initially positioned at 25 cm from the test section bottom, and then in succession 50 cm, 74 cm, and 99 cm. From each of these positions, the probe was moved downward 9750 steps at a rate of 300 steps per second which synchronized data collection at a rate of 100 samples per second. The probe velocity was 3.3 cm/s as compared to the bulk vertical velocity of 0.2 cm/s at which these experiments were conducted. Separate tests confirmed there was no significant effect of a traverse through the gradient layer on the subsequent gradient layer evolution.

2.3. Flow visualization

Visualizations of the flow and density fields were performed with hydrogen bubble and shadow-graph techniques. In both cases, a divide-by-n circuit was used to operate a Nikon FM2 camera at a selected frame rate. Images were also recorded with a video camera. The hydrogen bubble generator was based largely on the circuit described by Budwig and Peattie (1989). The visualization experiments were performed with 0.05 mm diameter chromel wire which produced uniformly fine bubbles that reflect light well enough to be readily visible. Lighting was provided by two slide projectors located approximately 55° off of the line of sight and focused at the bubble wire position.

The shadowgraph experiments were performed by lighting the back of the test section with two slide projectors. Mylar paper was placed on the front of the test section on which the shadowgraph images were then visible.

3. Results and discussion

Experiments were performed with flow rate as the primary control variable. The matrix of tests in which local density was measured is shown in Table 1.

Due to the low mass diffusivity of sodium chloride in water, the system Péclet number, defined as

$$Pe \equiv \frac{v_b H}{\alpha_m} = \frac{\dot{V} H}{\alpha_m L W}, \tag{1}$$

is of the same scale as those typical of large-scale thermal storage vessels. The densimetric or internal Froude number, defined as

$$Fr = \frac{\bar{u}_i}{\sqrt{g'h}}, \tag{2}$$

is of order one and therefore indicates gravitational effects are of first-order significance. The jet Reynolds number is defined as

$$Re = \frac{\bar{u}_i h}{\nu}. \tag{3}$$

As defined, the Péclet number reflects the magnitude of the diffusional time scale relative to that of the time scale of the filling process whereas the Froude and Reynolds numbers reflect local jet quantities.

The output voltage of the conductivity instrument is proportional to local conductivity and for the present range of salinities, is therefore also proportional to specific gravity. Thus, since the specific gravity as measured by the hydrometer is proportional to water at a reference temperature of 15.6 °C, the dimensionless density is simply

$$\rho = \frac{\hat{\rho} - \hat{\rho}_l}{\hat{\rho}_h - \hat{\rho}_l} = \frac{V - V_l}{V_h - V_l} \tag{4}$$

where $\hat{\rho}_l$ and $\hat{\rho}_h$ are the dimensional densities of the low and high density inflow solutions, respectively, and V_l and V_h are the corresponding output voltages. Since, in all cases, $\hat{\rho}_h$ and $\hat{\rho}_l$ were held constant, the dimensionless densities may be compared directly.

3.1. Density traces

The fixed probe experiments consisted of measuring the local density at a fixed position throughout the duration of the filling process. In all cases, the probe was positioned at the mid point of the test section in the $\hat{x}$ and $\hat{z}$ directions, $x = \hat{x}/L = 0.5$ and $z = \hat{z}/W = 0.5$. In addition, the vertical position of the probe was held constant at $y_p = \hat{y}_p/H =$

Table 1
Experimental test matrix for the fixed and moving probe data

$\dot{V}$ (lpm)	Type[a]	$\hat{u}_i$ (cm/s)	$\hat{t}_c$ (s)	$\hat{t}_f$ (s)	Pe	Fr	Re	No.
3.2	F	0.43	11.7	6327	0.16×10^6	0.062	0.22×10^3	3
15.5	F	2.1	2.42	1312	0.78	0.297	1.06	4
26.5	F	3.5	1.42	768	1.35	0.508	1.81	4
26.5	M	3.5	1.42	768	1.35	0.508	1.81	12
31.4	F	4.2	1.20	648	1.60	0.602	2.15	4

The last column refers to the number of experiments performed at the given flow rate.

[a] The letter "F" represents fixed probe data sets and the letter "M" represents moving probe data sets.

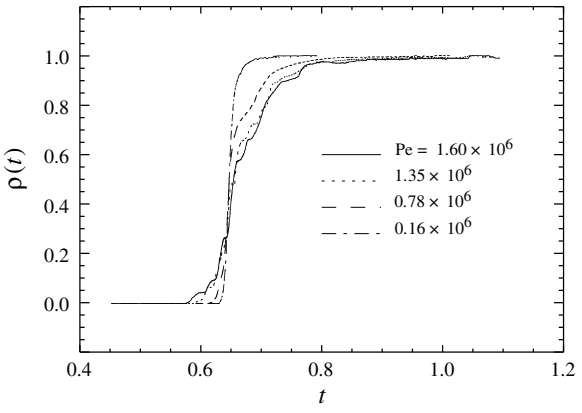

Fig. 3. Density traces $\rho(t, y_p)$, at several flow rates for $y_p = 0.65$.

0.65. The time coordinate is scaled by the time scale of the filling process so that a dimensionless time may be defined as

$$t = \frac{\hat{t}}{\hat{t}_f} \tag{5}$$

where $\hat{t}_f = H/\bar{v}_b$.

Density traces, $\rho(t, y_p)$, at several flow rates are shown in Fig. 3.

Since the bulk flow is aligned with the y-coordinate direction, the outlet (or upper) side of the gradient layer is first transported past the measurement probe. The impact of increased flow rate is plainly evident both in an apparent thickening of the gradient layers and in the level of local unsteadiness evident in the time trace.

3.2. Flow visualizations

The flow visualizations were undertaken to shed light on the nature of the flow in the gradient layer and the source of the unsteadiness observed in the density traces. Shadowgraph visualizations of the gradient layers at $Pe = 1.58 \times 10^6$ are shown in Fig. 4, at two separate instants. In the first image, a solitary wave is evident on the upper side of the gradient layers, moving from right to left. In the second image, the wake left by the passage of this solitary wave remains evident. The presence of the solitary wave is due to the turning of the gravity current at the enclosure wall after its initial passage across the width of the test section (Homan and Soo, 1997). The solitary wave generated by this turning of the gravity current is very similar to the solitary waves generated by the impulsive release of a fluid volume at an internal gradient layer with either a potential energy excess or deficit relative to the ambient stratification (Kao and Pao, 1979; Maxworthy, 1980). More than simply noting the presence of this motion, the physical scale should also be recognized. Estimating from the tick marks spaced at 2.5 cm intervals, the size of the solitary wave bulge is approximately that of the inlet height, at a time when the fill line has already moved over 5 inlet heights above the bottom of the test section. At the lower edge of the gradient layer, a great deal of unsteadiness is also evident. In fact, a shear layer is readily observed along which distinct vortices are evident. This shear is produced by the large-scale vortex driven by the jet inflow. Clearly, the strength of this recirculation is sufficient to produce local shear instabilities and a vertical distortion of the lower edge of the gradient layer at least as large as the inlet height.

Hydrogen bubble visualizations of the velocity field provide additional insight into the flow field in the region of the gradient layer. An image at $t = 0.32$ in a $Pe = 1.60 \times 10^6$ flow is shown in Fig. 5.

The image indicates clearly that the gradient layer is a region of large horizontal velocity components. Based on the bubble displacement and bubble pulse frequency, we have estimated the velocity magnitude to be 2.0 cm/s and 1.3 cm/s in the regions above and below the fill line with distinct bubble lines, respectively. These velocities are one-third to one-half of the inlet velocity at a vertical location over 7 times the inlet height above the floor of the test section. An image from a much later stage in the filling process, shown in Fig. 6, reveals velocities still a significant

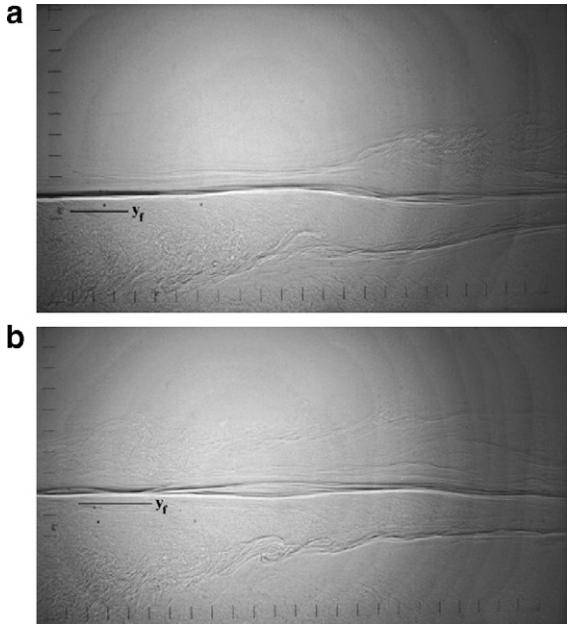

Fig. 4. Shadowgraph visualizations of the gradient layer showing solitary wave motion and shear instabilities at $Pe = 1.58 \times 10^6$ for (a) $t = 0.21$ and (b) $t = 0.23$. In both cases, the lower left corner of the grid axes are located at $x = (14.6\text{ cm})/L = 0.12$, $y = (13.3\text{ cm})/H = 0.11$ and the tick marks are spaced 2.5 cm apart.

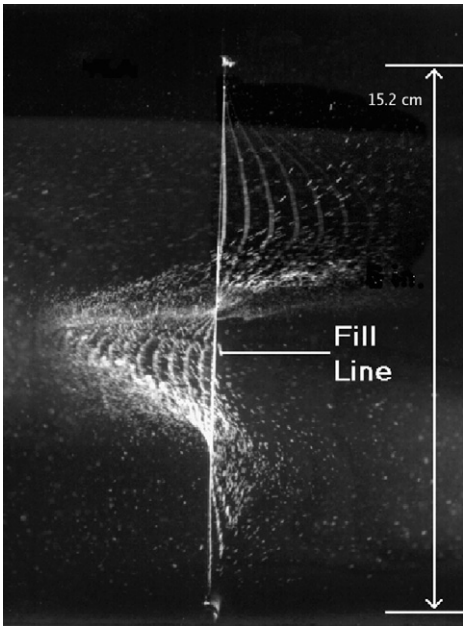

Fig. 5. Hydrogen bubble visualization of the gradient layer at $t = 0.32$ for $Pe = 1.60 \times 10^6$. The center of the vertical wire is at $\hat{x}/L = 63.5\text{ cm}/L = 0.54$ and $\hat{y}/H = 38.1\text{ cm}/H = 0.32$. The bubble pulse frequency is 3 Hz.

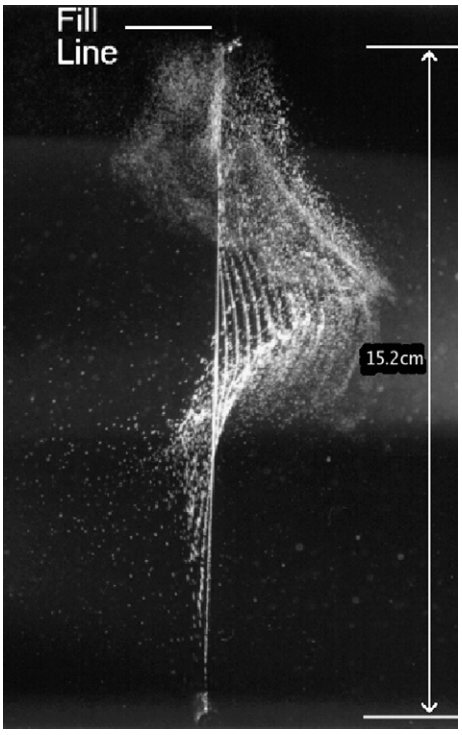

Fig. 6. Hydrogen bubble visualization of the gradient layer at $t = 0.71$ for $Pe = 1.60 \times 10^6$. The center of the vertical wire is at $\hat{x}/L = 63.5\,\text{cm}/L = 0.54$ and $\hat{y}/H = 76.2\,\text{cm}/H = 0.65$. The bubble pulse frequency is 4 Hz.

fraction of those at the inlet. The velocities in the region of distinct bubble line are approximately 1.0 cm/s at a time when the fill line is at a vertical position over 15 times that of the inlet height.

3.3. Time averaging

The flow and density fields are clearly composed of a wide range of length and time scales. Since, for the intended application, it is the large time scale variation which is of primary practical significance, we have utilized a time-averaging scheme to provide separation between the large and small time scales. Presuming that a suitable averaging period may be determined, the density trace may then be broken down as

$$\rho(t, y_\text{p}) = \bar{\rho}(t, y_\text{p}) + \rho'(t, y_\text{p}). \tag{6}$$

The present system clearly contains variations on at least two time scales, the time scale of the filling process, $\hat{t}_\text{f} = H/\bar{v}_\text{b}$, and the convective time scale, $\hat{t}_\text{c} = h/\bar{u}_\text{i}$. Based upon mass conservation and taking fluid volume to also be approximately conserved, the ratio of these time scales is related simply to geometry

$$\frac{\hat{t}_\text{f}}{\hat{t}_\text{c}} \simeq \left(\frac{W}{h}\right)^2 \left(\frac{H}{W}\right) = 576 \tag{7}$$

in the present investigation. We have found, and will show later, that a dimensionless averaging period,

$$P_\text{a} \equiv \frac{\widehat{P}_\text{a}}{\hat{t}_\text{c}}, \tag{8}$$

equal to 10 provides good separation of the large and small scale components of the density signal. Since $\log(\hat{t}_\text{f}/\hat{t}_\text{c}) = 3.82$, the selected averaging period corresponds to $\log(\hat{t}_\text{f}/\widehat{P}_\text{a}) = 1.76$, which is just slightly less than midway between the filling and convective time scales.

Alternatively, one may view the averaging in terms of a physical length scale, then

$$\hat{l}_\text{a} = v_\text{r} \widehat{P}_\text{a} \tag{9}$$

where v_r is the dimensional fill-line velocity relative to that of the probe. It is readily shown that $H/\hat{l}_\text{a} = \hat{t}_\text{f}/\widehat{P}_\text{a}$ and that the length scale of the averaging is nearly two orders of magnitude smaller than that of the enclosure height or, $\hat{l}_\text{a} \simeq 2$ cm.

While the convective and filling time scales are natural choices, additional time scales are certainly also present. The ratio of the convective time scale, $\hat{t}_\text{c}$ to the Kolmogorov time scale $\hat{\tau}$ (Tennekes and Lumley, 1972) for instance, simplifies to $\hat{t}_\text{c}/\hat{\tau} = Re^{1/2}$ and in the present experiments varies between 15 and 46. While the flow field in the enclosure is most certainly not uniformly turbulent, there are certain to be regions of turbulence or developing turbulence, given the fairly large jet Reynolds number. An additional time scale relevant to the present system is the buoyancy or Brunt–Vasaila frequency, defined as

$$N = \left(-\frac{g}{\hat{\rho}} \frac{\partial \hat{\rho}}{\partial \hat{z}}\right)^{1/2} \tag{10}$$

in Turner (1979). It is readily shown that the ratio of the convective time scale to N^{-1} is equal to the inverse Froude number. In the present experiments, the ratio of the convective time scale, $\hat{t}_\text{c}$, to the period of the oscillations at the buoyancy frequency, $2\pi/N$, varies from 0.2 to 3.8.

The average and perturbation traces at two different flow rates are shown in Fig. 7 and in Fig. 8.

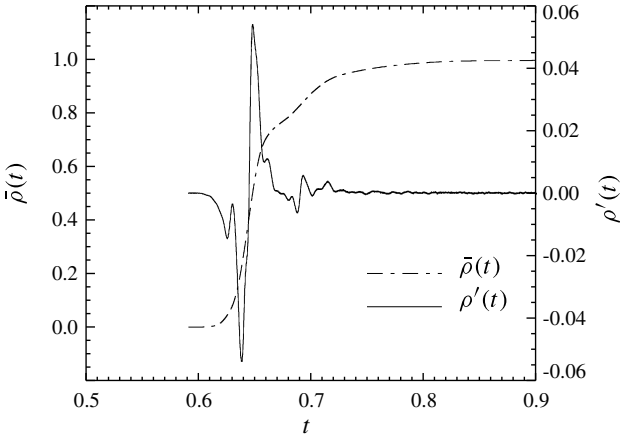

Fig. 7. Overlay of time-averaged density trace, $\bar{\rho}(t, y_\text{p})$, and perturbation trace, $\rho'(t, y_\text{p})$, for $Pe = 0.78 \times 10^6$, $y_\text{p} = 0.65$, and $P_\text{a} = 10$.

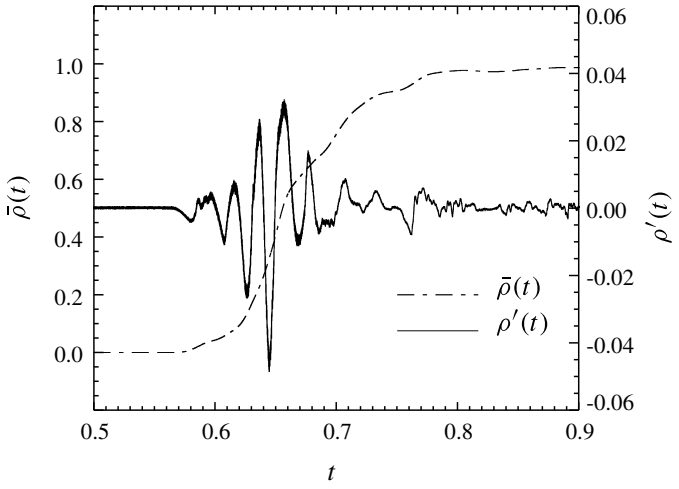

Fig. 8. Overlay of time-averaged density trace, $\bar{\rho}(t, y_p)$, and perturbation trace, $\rho'(t, y_p)$, for $Pe = 1.60 \times 10^6$, $y_p = 0.65$, and $P_a = 10$.

Note that in both figures, the ordinate scale of the perturbation component is a small fraction of the averaged component.

In both cases, the largest fluctuations occur during the passage of the gradient layer, $t \simeq y_p$. There is a distinct difference, however, in the nature of the density field above and below the gradient layer as fluctuations persist for much longer after the passage of the gradient layer than the extent to which they preceded the gradient layer. In addition, the higher flow rate trace shows significantly more high-frequency fluctuations than does the lower Péclet number trace.

3.4. Gradient layer thickness

The gradient layer thickness is computed relative to the fill-line position to obtain an instantaneous measure since the local thickness is clearly time-dependent. The outlet side thickness is defined as

$$\delta_o^*(t_o^*) = y_p(t_o^*) - y_f(t_o^*), \tag{11}$$

where $\delta_o^* \equiv \hat{\delta}_o^*/H$ and y_p and y_f are the probe and fill-line positions, respectively. The corresponding instant in time, t_o^*, is determined by

$$\bar{\rho}(t_o^*) = \Delta\rho_e \tag{12}$$

where $\Delta\rho_e$ is the edge density, generally taken between 0.05 and 0.25 (Homan, 2003). Similarly, on the inlet side of the gradient layer, the inlet side thickness is defined as

$$\delta_i^*(t_i^*) = y_f(t_i^*) - y_p(t_i^*) \tag{13}$$

and t_i^* is determined by

$$\bar{\rho}(t_i^*) = 1 - \Delta\rho_e. \tag{14}$$

As previously indicated, the dimensionless fill-line position is simply $y_f = t$ since the flow rate is constant in time. In the fixed probe experiments, the local density trace is of the form $\rho(t, y_p)$ and calculation of the instantaneous gradient layer thickness is straightforward. However, in the moving probe experiments, a local density profile of the form $\rho(t_p, y)$ is measured and the calculation of the gradient layer thickness must account for the time-dependent probe position. An important advantage however, is that with the moving probe experiments it is possible to compute the variation of the gradient layer thickness in time. In both the fixed and moving probe experiments, the uncertainty in the gradient layer thickness is dominated by the uncertainty in the volumetric flow rate. In the fixed probe experiments, the estimated uncertainty is between 1% and 3% of the enclosure height and, for the moving probe experiments, is up to 4% of the enclosure height. The larger uncertainty corresponds to the traverses taken in the later stages of the filling process due to the longer elapsed time from the start of the experiment.

The gradient layer thicknesses computed from all of the fixed probe cases indicated in Table 1 are shown in Fig. 9.

On the inlet side of the gradient layer, $\rho_e > 0.5$, the general trend is of increasing thickness with Péclet number. However, at the higher Péclet numbers, this is not uniformly true. At $\rho_e = 0.75$ for example, δ_i^* generally increases with Péclet number, however at $\rho_e = 0.95$, the highest Péclet number produces similar thicknesses as the next lower Péclet number. This general trend is consistent with the levels of mixing suggested by the flow visualizations at the higher Péclet numbers. Apparently, as the Péclet number increases, the rate of entrainment from the gradient layer increases and there is an increasing erosion of the gradient layer. The result of the entrainment is a lengthening of the "tail" of the gradient layer, particularly at densities approaching that of the inlet. This is consistent with observations made elsewhere, such as by Wildin (1996). On the outlet side of the gradient layer, the thickness increases with Péclet number for smaller ρ_e and shows no clear trend for $\rho_e = 0.25$. However, based on the results of the flow visualizations as well as the density perturbation traces, the interior of the gradient layer is strongly influenced by the presence of

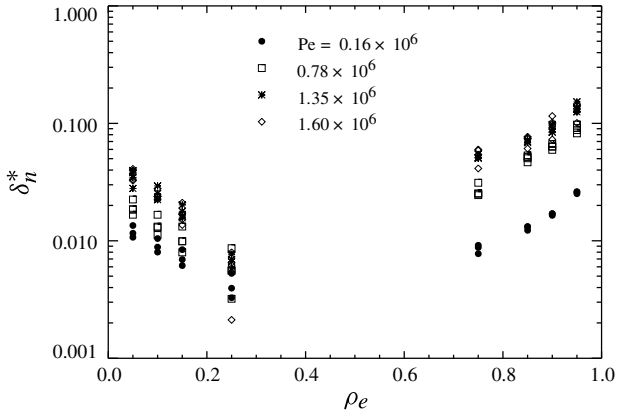

Fig. 9. Gradient layer thickness versus edge definition as determined from time-averaged density traces at probe position $y_p = 0.65$. The edge values, ρ_e, less than 0.5 correspond to the outlet side of the gradient layer and those greater than 0.5 to the inlet side of the gradient layer.

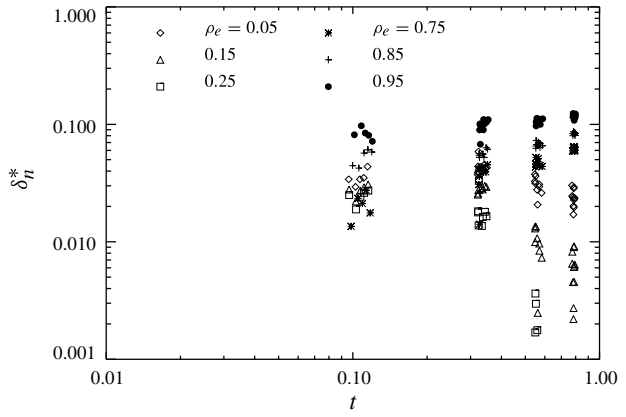

Fig. 10. Gradient layer thickness evolution, $\delta_n^*(t)$, as determined from density profiles at $Pe = 1.35 \times 10^6$ for select edge definitions. The edge values, ρ_e, edges less than 0.5 correspond to the outlet side of the gradient layer and those greater than 0.5 to the inlet side of the gradient layer.

large-amplitude internal waves, the detailed character of which varies with Péclet number.

These observations are further reinforced by consideration of the moving probe data which provides an even clearer indication of gradient layer evolution. The instantaneous gradient layer thicknesses for the moving probe cases are shown in Fig. 10.

As before, the edge values less than 0.5 correspond to the outlet side of the gradient layer, whereas $\rho_e > 0.5$ corresponds to the lower or inlet side of the gradient layer.

Table 2
The impact of averaging period, $P_a = \widehat{P}_a/\hat{t}_c$, on the computed gradient layer thickness, δ_n^*, as determined from $\bar{\rho}(t)$ for the fixed probe cases

ρ_e	Pe	δ_n^*			
		$P_a = 1$	5	10	25
0.05	1.63×10^5	0.0100	0.0111	0.0135	0.0233
	7.88	0.0213	0.0216	0.0225	0.0290
	1.35×10^6	0.0388	0.0390	0.0396	0.0437
	1.60	0.0362	0.0353	0.0334	0.0381
0.15	1.63×10^5	0.00604	0.00663	0.00840	0.0162
	7.88	0.0111	0.0119	0.0132	0.0194
	1.35×10^6	0.0233	0.0219	0.0202	0.0223
	1.60	0.0180	0.0167	0.0136	0.0157
0.75	1.63×10^5	0.00573	0.00630	0.00776	0.0142
	7.88	0.0250	0.0251	0.0251	0.0251
	1.35×10^6	0.0528	0.0533	0.0545	0.0532
	1.60	0.0596	0.0594	0.0588	0.0601
0.85	1.63×10^5	0.0102	0.0107	0.0123	0.0198
	7.88	0.0459	0.0463	0.0466	0.0480
	1.35×10^6	0.0700	0.0707	0.0724	0.0763
	1.60	0.0737	0.0749	0.0770	0.0825
0.95	1.63×10^5	0.0243	0.0252	0.0260	0.0317
	7.88	0.0823	0.0821	0.0822	0.0842
	1.35×10^6	0.154	0.153	0.152	0.150
	1.60	0.138	0.139	0.143	0.148

The ρ_e edges less than 0.5 correspond to the outlet side of the gradient layer, δ_o^*, and those greater than 0.5 to the gradient layer thickness on the inlet side, δ_i^*.

Remarkably, the outer edges of the gradient layer on the inlet side increase relatively slowly in time. However, the $\rho_e = 0.75$ edge increases sharply in time. The outer edge of the gradient layer on the upper side of the gradient layer is expanding slowly, if at all. Although clearly asymmetric, the $\rho_e = 0.05$ and 0.95 edges are both evolving relatively slowly in time. On the other hand, the interior of the gradient layer changes significantly during the filling process. The mechanism for this continuing evolution is likely the internal wave motion evident in the flow visualizations.

As previously indicated, the instantaneous gradient layer thicknesses are computed from the averaged density traces. A key element is the averaging period used to separate the full density signal into average and perturbation components. As already shown in Figs. 7 and 8, a dimensionless averaging period $P_a = 10$ gives a suitable separation of the short and long time scale components. The impact of this averaging on the computed instantaneous gradient layer thickness is shown in Table 2.

An overly long averaging period, $P_a = 25$ for example, in many cases has an appreciable impact on the computed thickness. The effect is one of oversmoothing what are in fact relatively sharp gradient layer edges.

3.5. Quantifying gradient layer evolution

The flow visualizations have demonstrated the importance of multi-dimensional fluid motion to the evolution of the gradient layer even though the measured density profiles, at first glance, have some semblance to one-dimensional diffusional growth. However, the observed thicknesses are much greater than can be explained by molecular diffusivities. In addition, as indicated by the measured density traces and profiles, the gradient layer may also be strongly asymmetric and exhibits growth rates other than what would be expected by one-dimensional molecular diffusion, that is $\delta^* \sim \sqrt{t/Pe}$. Thus, even if one focuses attention on the area-averaged temperature, as would be of most interest to practical thermal storage applications, empirical observations indicate a strong impact of the multi-dimensional fluid motion. The impact of this motion presents itself in the perturbation integral appearing in the horizontally-averaged energy equation,

$$\frac{\partial \overline{T}}{\partial t} + \frac{\partial \overline{T}}{\partial y} = \frac{\partial}{\partial y}\left(\frac{1}{Pe}\frac{\partial \overline{T}}{\partial y} - \int_{A_c} v'T'\,\mathrm{d}A\right). \tag{15}$$

The horizontally-averaged temperature is defined as $\overline{T}(t,y) = T(t,\mathbf{x}) - T'(t,\mathbf{x})$. The perturbation integral represents the impact of the multi-dimensional fluid motion on the evolution of the horizontally-averaged temperature. In effect, a closure problem has been introduced which demands a suitable characterization for the perturbation integral. Presuming that the perturbation integral is proportional to the gradient in mean temperature leads naturally to the introduction of a diffusivity, denoted by ε

and termed a convective diffusivity (Homan and Soo, 1997), defined by

$$\frac{\varepsilon}{v_b H}\frac{\partial \overline{T}}{\partial y} = -\int_{A_c} v' T' \, dA. \tag{16}$$

Introducing this definition into the energy equation results in an expression for the evolution of the area-averaged temperature distribution,

$$\frac{\partial \overline{T}}{\partial t} + \frac{\partial \overline{T}}{\partial y} = \frac{\partial}{\partial y}\left(\frac{\kappa}{Pe}\frac{\partial \overline{T}}{\partial y}\right), \tag{17}$$

where $\kappa \equiv 1 + \varepsilon/\alpha$. The utility of this approach clearly depends on a suitable characterization for the convective diffusivity ε, or alternatively the diffusivity ratio κ. The practical significance of κ is that it reflects the size of the apparent diffusivity resulting from multi-dimensional fluid motion at the gradient layer relative to one-dimensional molecular diffusion. Thus, in the limit of vanishing multi-dimensional effects, κ is unity and the growth of the gradient layer is that dictated by one-dimensional diffusion alone. Attention will therefore be focused on the extent to which (a) uniform diffusivity, (b) constant but non-uniform diffusivity, and (c) transient non-uniform diffusivity reflects the empirically observed behaviors. These three parameterizations of κ have been developed in Homan (2003) using an integral analysis and compared to previously published data.

A straightforward approach to quantifying the evolution of the gradient layer is to consider a time-invariant uniform diffusivity which reflects the impact of the multi-dimensional fluid motion on the evolution of the gradient layer, as first proposed in Homan et al. (1996). An average convective mixing factor, κ_a, may then be readily computed from the analytical result for one-dimensional diffusion, $\delta_a^* = 2c\sqrt{t_a/(Pe/\kappa_a)}$. The mixing factor, or diffusivity ratio, is then given by

$$\kappa_a = \frac{Pe}{t_a}\left(\frac{\delta_a^*}{2c}\right)^2, \tag{18}$$

where the required empirical input is an average gradient layer thickness at a specific instant, $\delta_a^*(t)$. The convective mixing factor, κ_a is then related to the effective diffusivity by $\kappa_a \equiv 1 + \varepsilon_a/\alpha_m$ where ε_a is the average convective diffusivity and α_m is the molecular diffusivity. The constant c depends only on $\Delta\rho_e$ and is given approximately by $c = 1.46 - 0.36(33.2\Delta\rho_e - 1.0)^{1/2}$ (Homan and Soo, 1998). The mixing factors computed from all of the density traces and profiles are shown in Tables 3 and 4, respectively.

While an average mixing factor is readily estimated, this model does not capture several key aspects of the empirically observed behavior since it predicts a symmetric profile with a gradient layer thickness growing proportional to $t^{1/2}$. This is evident in the fact that κ_a takes on different values at different instants in time, as seen in Table 4. Essentially, κ_a reflects the *average* diffusivity ratio from the start of the filling process to the selected time t. Nonetheless, both the density trace and density profile data

Table 3
Overall parameters computed from the density trace, $\rho(t, y_p)$, data sets

$\Delta\rho_e$	Pe	κ_a	$\frac{t_u^*}{t_l^*}\left(\frac{\delta_l^*}{\delta_u^*}\right)^2$	κ_r	κ_i
0.25	0.163×10^6	1.64×10^1	4.88	0.171	9.29
	0.788×10^6	6.28×10^2	33.9	0.128	3.95×10^2
	1.35×10^6	2.61×10^3	54.8	0.124	2.46×10^3
	1.60×10^6	2.91×10^3	33.4	0.111	3.05×10^3
0.15	0.163×10^6	1.15×10^1	3.35	4.29×10^{-2}	10.4
	0.788×10^6	4.97×10^2	25.2	3.45×10^{-2}	7.20×10^2
	1.35×10^6	1.75×10^3	14.4	3.58×10^{-2}	2.31×10^3
	1.60×10^6	2.12×10^3	18.4	3.52×10^{-2}	2.87×10^3
0.05	0.163×10^6	1.08×10^1	4.51	7.71	42.2
	0.788×10^6	3.31×10^2	20.1	2.89×10^{-3}	1.21×10^3
	1.35×10^6	1.82×10^3	12.2	2.94×10^{-3}	4.48×10^3
	1.60×10^6	2.10×10^3	10.6	37.9	1.76×10^4

For each of the density traces, the probe was maintained at a fixed position, $y_p = 0.65$.

Table 4
Overall parameters computed from the density profile, $\rho(t_p, y)$, data sets

$\Delta\rho_e$	t	κ_a	$\frac{t_u^*}{t_l^*}\left(\frac{\delta_l^*}{\delta_u^*}\right)^2$	κ_r	κ_i	$\left(\frac{t_u^*}{t_l^*}\right)^{(1+b)}\left(\frac{\delta_l^*}{\delta_u^*}\right)^2$	$\tilde{\kappa}_r$	$\tilde{\kappa}_i$
0.25	0.11	7.99×10^3	0.808	2.12	9.44×10^3	0.818	2.06	2.15×10^3
	0.33	3.65×10^3	4.76	0.173	2.55×10^3	4.78	0.172	1.25×10^3
	0.56	2.05×10^3	1.66×10^4	0.112	2.40×10^3	1.67×10^4	0.112	1.65×10^3
	0.79	1.58×10^3	4.36×10^2	0.115	3.00×10^3	4.37×10^2	0.115	2.57×10^3
0.15	0.11	9.09×10^3	3.58	0.042	8.70×10^3	3.66	0.042	2.04×10^3
	0.33	3.10×10^3	3.62	0.042	2.78×10^3	3.65	0.042	1.36×10^3
	0.56	1.61×10^3	1.38×10^2	0.032	2.67×10^3	1.39×10^2	0.032	1.84×10^3
	0.79	1.56×10^3	3.07×10^2	0.032	2.94×10^3	3.08×10^2	0.032	2.52×10^3
0.05	0.11	6.67×10^3	5.86	11.54	2.55×10^4	6.05	12.2	6.10×10^3
	0.33	3.16×10^3	5.16	9.45	1.03×10^4	5.22	9.63	5.09×10^3
	0.56	1.38×10^3	13.1	2.91×10^{-3}	3.76×10^3	13.1	2.91×10^{-3}	2.59×10^3
	0.79	1.43×10^3	25.2	2.87×10^{-3}	3.32×10^3	25.4	2.87×10^{-3}	2.84×10^3

For each of the density profiles, the traverse through the density profile occurs over a relatively short period, $t \simeq t_p$.

indicate that κ_a scales with Pe, consistent with a more strongly forced flow field. Further, the mixing factor grows to several orders of magnitude larger than one, indicating an ever stronger impact of multi-dimensional fluid motion.

Another point of comparison for the empirical data is the dimensionless density at the fill line. If the profile was fully described by one-dimensional diffusion with a constant diffusivity, the fill-line density would be $\bar{\rho}_f = \bar{\rho}(t_f, y_p) \equiv 0.5$. Fig. 11 shows the average density at the instant the fill line passes the fixed probe. Clearly there is some scatter, even at a specific Péclet number. However, the general trend appears to be $\bar{\rho}_f < 0.5$. At the very least, this provides another indication of the dynamic state of the gradient layer, even at vertical positions of $y_p = 0.65$, which is well above the inlet.

A model which captures the observed asymmetry in the density profiles is a constant but non-uniform diffusivity, resulting in $\kappa_u \neq \kappa_l$. The ratio of the two mixing factors, $\kappa_r = \kappa_l/\kappa_u$, determines the predicted fill-line density and is given by

$$\kappa_r = \left[\frac{\rho_f}{1-\rho_f}\right]^2. \tag{19}$$

In addition,

$$\kappa_r = \frac{(Pe/t_l)(\delta_l^*/r_l)^2}{(Pe/t_u)(\delta_u^*/r_u)^2} = \left(\frac{r_u}{r_l}\right)^2 \frac{t_u}{t_l}\left(\frac{\delta_l^*}{\delta_u^*}\right)^2, \tag{20}$$

where r_u and r_l depend only on $\Delta\rho_e$ and ρ_f (Homan, 2003) and are given by

$$\begin{aligned} r_u &= 1 - \left(\frac{\Delta\rho_e}{\rho_f}\right)^{1/2}, \\ r_l &= -1 + \left(\frac{\Delta\rho_e}{1-\rho_f}\right)^{1/2}. \end{aligned} \tag{21}$$

Equating the two expressions for κ_r, Eqs. (19) and (20), and bringing the empirical parameters to one side,

$$\frac{t_u}{t_l}\left(\frac{\delta_l^*}{\delta_u^*}\right)^2 = \left[\frac{\rho_f}{1-\rho_f}\right]^2\left(\frac{r_u}{r_l}\right)^2. \tag{22}$$

The right-hand side of this expression may then be recognized as a function which depends only on $\Delta\rho_e$ and ρ_f,

$$f(\rho_f; \Delta\rho_e) \equiv \left[\frac{\rho_f}{1-\rho_f}\right]^2\left(\frac{r_u}{r_l}\right)^2, \tag{23}$$

where $\Delta\rho_e \leqslant \rho_f \leqslant 1 - \Delta\rho_e$. The significance of this function is that it determines the fill-line density necessary to match a measured $\delta_n^*(t_n)$ pair for a specific edge value, $\Delta\rho_e$. Fig. 12 shows a plot of this function based on the quadratic profiles utilized in Homan (2003). Thus, once $\delta_u^*(t_u)$ and $\delta_l^*(t_l)$ are measured for a particular $\Delta\rho_e$, ρ_f is specified, κ_r follows from (19) and

$$\kappa_n = \frac{Pe}{at_n}\left(\frac{\delta_n^*}{r_n}\right)^2, \tag{24}$$

where n is either of 'u' or 'l' and the coefficient a is equal to 12.

The required pair of empirical gradient layer thicknesses may be determined from both the density trace and the density profile data. The results are shown in Tables 3 and 4. The improved description of the data is evident, for both the density trace and density profile data, in the smaller variation of κ_i with time. Of course, once again, the remaining time dependency of κ_r and κ_i indicate that the time variation of the gradient layer thickness is not strictly $\delta^* \propto \sqrt{t}$.

While the constant diffusivity ($\kappa_r \neq 1$) model captures the asymmetry observed in measured profiles, it still predicts a gradient layer thickness which varies as $t^{1/2}$. However, this is not generally true for measured profiles, as evident in the current results and those published in the literature (Truman et al., 1985; Wildin and Sohn, 1993; Zurigat et al., 1991, 1989). One means of modeling growth rates in δ^* other than $t^{1/2}$, is to introduce a transient diffusivity of the form

$$\kappa(t) = \tilde{\kappa}(1+b)t^b, \tag{25}$$

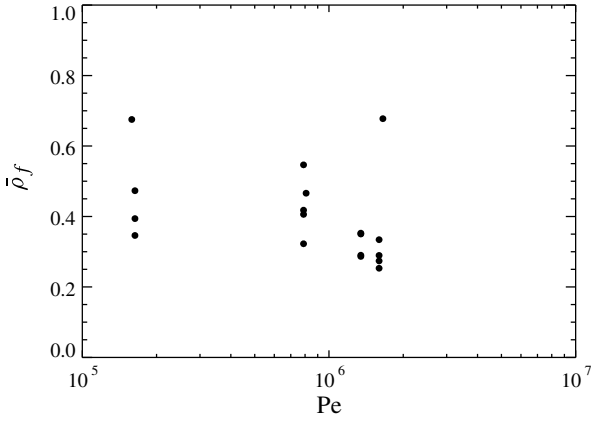

Fig. 11. Variation of fill-line density, $\bar{\rho}_f$, versus Péclet number for the fixed probe experiments as computed from $\bar{\rho}_f = \bar{\rho}(t = t_f, y = y_p)$.

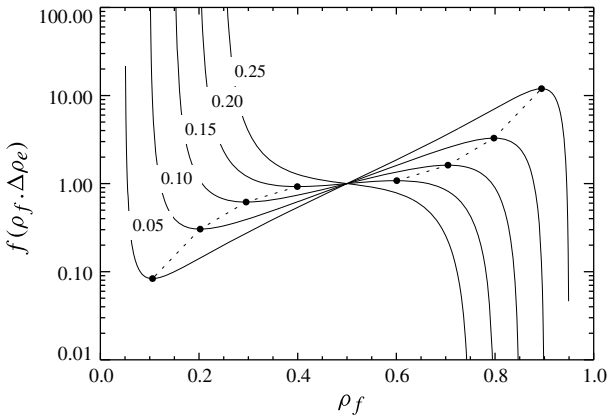

Fig. 12. Thickness function, $f(\rho_f, \Delta\rho_e)$, versus fill-line density, ρ_f.

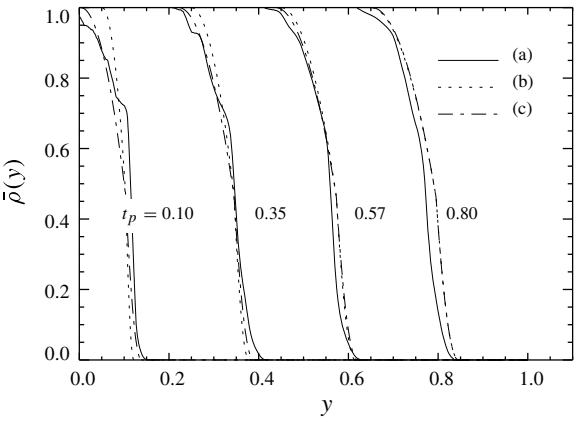

Fig. 13. Time-averaged density profile evolution, $\bar{\rho}(t_p, y)$ as (a) measured and as predicted by the (b) constant diffusivity and (c) transient diffusivity models. The parameters of the constant diffusivity model are $\kappa_i = 3000$ and $\kappa_r = 8.6$. The parameters for the transient diffusivity model are $b = -0.65$, $\tilde{\kappa}_i = 2500$ and $\tilde{\kappa}_r = 8.3$.

which then predicts a gradient layer thickness growing according to

$$\delta_n^* = \left[\frac{a\tilde{\kappa}_n t^{(1+b)} r_n}{Pe}\right]^{1/2}, \tag{26}$$

where r_n remains as defined in (21). In spite of the fact that κ_n is now time-dependent, the diffusivity ratio, $\tilde{\kappa}_r$ remains constant and $\tilde{\kappa}_r = \tilde{\kappa}_l/\tilde{\kappa}_u$. The required empirical data is now the constant b in the power law relation $\delta^* \propto t^{(1+b)/2}$ and the gradient layer thickness pair, $\delta_n^*(t_n)$. The exponent b can be readily determined from a plot of $\delta_n^*(t)$, such as in Fig. 10. In the present investigation, this is available only from the multiple density profiles since the density traces were taken at only a single point. However, density traces at multiple vertical positions would also be equally suitable for determination of b.

The parameters in the transient diffusivity model are shown in Table 4 as computed from the density profile data. The value for the exponent b was computed from the $\delta_i^*(t)$ data for $\Delta\rho_e = 0.05$. This corresponds to the $\rho = 0.95$ edge of the gradient layer. The time variation of the constants in the model, $\tilde{\kappa}_r$ and $\tilde{\kappa}_i$, is less than for either of the uniform and non-uniform diffusivity models, thereby indicating an improved description of the gradient layer evolution. Further confirmation of the improved prediction is shown by the overlay, in Fig. 13.

4. Conclusions

Measurements of the density profile in a stably-stratified open enclosure have shown the evolution of the internal gradient layer to be strongly time-dependent. Visualizations of the density and velocity fields have indicated that the evolution of the gradient layer results from a complex interaction between the internal wave structure and jet-driven shear. The nature of the unsteadiness includes a wide range of length and time scales spanning that of the filling process down to that of the local shear instabilities produced at the gradient layer. In order to separate the observed range of time scales, the local density trace was time-averaged over a period midway between the time scale of the filling process and the convective and buoyant time scales. However, even the time-averaged density profile displays a complex evolution in time which is not suitably described by simple one-dimensional molecular diffusion. A means is introduced for computing instantaneous gradient layer thicknesses from both density trace and density profile data. Utilizing an integral model incorporating transient and non-uniform effective diffusivities, model parameters were estimated from the computed gradient layer thicknesses and compared to the experimental profiles. The results show that these effective diffusivities are orders of magnitude larger than simple molecular diffusion and scale with Péclet number. However, as might be expected, at low flow rates the effective diffusivity produced by the multi-dimensional fluid motion diminishes. The quantitative results are useful for estimation of gradient layer thicknesses in the sizing of stratified thermal storage devices and for the modeling of gradient layer evolution in these same devices.

References

Anderson, R., Kreith, F., 1987. Natural convection in active and passive solar thermal systems. In: Irvine, T.F., Jr., Hartnett, J.P. (Eds.), Advances in Heat Transfer, vol. 18. Academic Press, pp. 1–86.

Budwig, R., Peattie, R., 1989. Two new circuits for hydrogen bubble flow visualization. J. Phys. E, Sci. Instrum. 22, 250–254.

Catton, I., 1978. Natural convection in enclosures. In: Proceedings of the Sixth International Heat Transfer Conference. vol. 6, pp. 13–31.

Head, M.J., 1983. The use of miniature four-electrode conductivity probes for high resolution measurement of turbulent density or temperature variations in salt-stratified water flows. Ph.D. Thesis, University of California San Diego.

Homan, K.O., 2003. Integral solutions for transient temperature profiles in stably-stratified open enclosures. ASME J. Heat Transfer 125, 273–281.

Homan, K.O., Sohn, C.W., Soo, S.L., 1996. Thermal performance of stratified chilled water storage tanks. Int. J. HVAC & R. Res. 2, 158–170.

Homan, K.O., Soo, S.L., 1997. Model of the transient stratified flow into a chilled water storage tank. Int. J. Heat Mass Transfer 40, 4367–4377.

Homan, K.O., Soo, S.L., 1998. Laminar flow efficiency of stratified chilled-water storage tanks. Int. J. Heat Fluid Flow 19, 69–78.

Hyun, J.M., 1994. Unsteady buoyant convection in an enclosure. In: Irvine, T.F., Jr.Jr., Hartnett, J.P., Cho, Y.I. (Eds.), Advanced of Heat Transfer, vol. 24. Academic Press, pp. 277–320.

Ji, Y., Homan, K.O., 2006. Transition from gravity- to inertia-dominated behavior computed for the turbulent stably-stratified filling of an open enclosure. Int. J. Heat Fluid Flow 27, 490–501.

Ji, Y., Homan, K.O., 2007. On simplified models of the rate- and time-dependent performance of stratified thermal storage. ASME J. Energy Resour. Technol. 129, 214–222.

Kao, T.W., Pao, H.-P., 1979. Wake collapse in the thermocline and internal solitary waves. J. Fluid Mech. 97, 115–127.

Lavan, Z., Thompson, J., 1977. Experimental study of thermally stratified hot water storage tanks. Solar Energy 19, 519–524.

Mavros, P., Belessiotis, V., Haralambopoulos, P., 1994. Stratified energy storage vessels: characterization of performance and modeling of mixing behavior. Solar Energy 52, 327–336.

Maxworthy, T., 1980. On the formation of nonlinear internal waves from the gravitational collapse of mixed regions in two and three dimensions. J. Fluid Mech. 96, 47–64.

Neiswanger, L., Johnson, G.A., Carey, V.P., 1987. An experimental study of high Rayleigh number mixed convection in a rectangular enclosure with restricted inlet and outlet openings. ASME J. Heat Transfer 109, 446–453.

Ostrach, S., 1982. Natural convection heat transfer in cavities and cells. In: Proceedings of the Seventh International Heat Transfer Conference. vol. 1, pp. 365–379.

Tennekes, H., Lumley, J.L., 1972. A First Course in Turbulence. The MIT Press, Cambridge, MA.

Truman, C.R., Wildin, M.W., Yoo, J., 1985. Scale modeling of stratified water thermal storage tanks. In: Proceedings of Symposium on Modeling Environmental Flows, ASCE/ASME Mechanics Conference, pp. 93–102.

Turner, J.S., 1979. Buoyancy Effects in Fluids. Cambridge University Press.

Wildin, M.W., 1996. Experimental results from single-pipe diffusers for stratified thermal energy storage. ASHRAE Trans. 102 (2), 123–132.

Wildin, M.W., Sohn, C.W., 1993. Flow and temperature distribution in a naturally stratified thermal storage tank. USACERL Technical Report FE-94/01, U.S. Army Construction Engineering Research Laboratories.

Zurigat, Y.H., Liche, P.R., Ghajar, A.J., 1991. Influence of inlet geometry on mixing in thermocline thermal energy storage. Int. J. Heat Mass Transfer 34, 115–125.

Zurigat, Y.H., Maloney, K.J., Ghajar, A.J., 1989. A comparison study of one-dimensional models for stratified thermal storage tanks. ASME J. Solar Energy Eng. 111, 204–210.